Materials & Design 216 (2022) 110557

Contents lists available at ScienceDirect

Materials & Design

journal homepage: www.elsevier.com/locate/matdes

Revealing the AC electromechanically coupled effects and stable sensitivity on the dielectric loss in CNT-based nanocomposite sensors

Xiaodong Xia [a,*], Shijun Zhao [a], Huiming Yin [b], George J. Weng [c,*]

[a] School of Civil Engineering, Central South University, Changsha 410083, PR China
[b] Department of Civil Engineering and Engineering Mechanics, Columbia University, New York, NY 10027, USA
[c] Department of Mechanical and Aerospace Engineering, Rutgers University, New Brunswick, NJ 08903, USA

HIGHLIGHTS

- Demarcating CNT-based nanocomposite sensor via the dielectric loss possesses the advantage of stable sensitivity over the traditional electric resistance.
- The electromechanical mechanism of CNT/PVDF nanocomposite sensor is quantitatively illustrated over broad strain range ($0 \sim 10\%$) and frequency spectrum ($5 \sim 500$ kHz).
- The effective dielectric loss change ratio and strain-sensitivity factor are predicted by a homogenization scheme and validated by experimental data.
- The developed theory directly determines the dielectric loss change ratio and further simplifies the design procedure of highly-sensitive strain sensors.

GRAPHICAL ABSTRACT

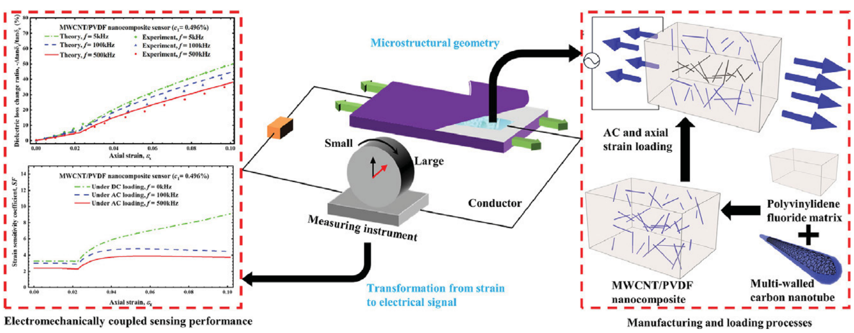

ARTICLE INFO

Article history:
Received 20 November 2021
Revised 12 March 2022
Accepted 14 March 2022
Available online 16 March 2022

Keywords:
CNT-based nanocomposite sensors (CNCSs)
Electromechanically coupled
AC frequency
Dielectric loss
Sensitivity analysis

ABSTRACT

This work is concerned with the characterization of load-dependent dielectric loss and sensitivity analysis for CNT-based nanocomposite sensors (CNCSs) under AC loading. To this end, an electromechanically coupled microstructural theory is developed from the bottom up to quantitatively predict their overall dielectric loss change ratio and strain-sensitivity factor. In the theory, various categories of load-dependent functional interface effects, such as strain- and filler-dependent electron hopping and dielectric relaxation, are incorporated into it. The electric damage process under mechanical load is characterized through the principle of irreversible thermodynamics. The outcome is a microstructure-based coupled theory whose predictions of AC dielectric loss change ratio can be directly calibrated with the experimental data of MWCNT/PVDF nanocomposite sensor over a broad strain loading range from 0 to 10% and a wide frequency spectrum from 5 kHz to 500 kHz, where PVDF is a shape memory polymer. The theory further demonstrates the advantage of demarcating CNCSs via the dielectric loss over the traditional electric resistance. It can be used to rapidly determine the macroscopic dielectric loss change ratio by choosing a specific CNT volume concentration and AC working frequency, and further simplify the design procedure of highly sensitive strain sensors.

* Corresponding authors.
E-mail addresses: xiaodongxia@csu.edu.cn (X. Xia), gjweng@soe.rutgers.edu (G.J. Weng).

https://doi.org/10.1016/j.matdes.2022.110557
0264-1275/

1. Introduction

With the rapid development of intelligent technology during the information era, it arises the growing needs to precisely sense the surrounding environment in daily life [1]. As a crucial component in monitoring systems, smart sensors have built up tight connections between the physical world and the digital system by transferring the monitored information to electrical or digital signals [2]. Specifically, the strain sensors can quantitively monitor the mechanical strain of the material point via measuring electrical signals [3–6]. This category of sensors has been extensively employed in the practical application of human–machine interfaces [7], structural health monitoring [8], electronic skin [9].

Conventional strain sensors are mainly classified into the silicon-based sensor and piezoelectric sensor. Among them, the silicon-based strain sensor takes the advantage of high sensitivity and large piezoresistive coefficients on account of the strong correlation of bandgap in regard to the inter-atomic spacing [2]. However, this category of strain sensors is prone to break with low fracture toughness due to the intrinsic brittleness and stiffness of semiconductor materials [10]. As an alternative, the piezoelectric strain sensor is fabricated by functionalized ceramics or polymers with a high performance of piezoelectricity [11]. However, it works merely under a narrow strain measuring range while consuming ultrahigh manufacturing costs [12]. Distinguished from the former two categories of strain sensors, CNT-based nanocomposite sensors (CNCSs) have been manufactured by adding CNT nanofillers into polymer matrix. Jang et al. [13] investigated the influences of ferromagnetic particles on the sensitivity of multi-walled carbon nanotube (MWCNT)/ polydimethylsiloxane (PDMS) nanocomposites. Abraham et al. [14] fabricated the MWCNT/ styrene butadiene rubber (SBR) nanocomposites and applied them to manufacture the flexible solvent sensor. It possesses excellent piezoresistance performance [15] and flexible mechanical behavior [16] over a broad measuring range. Consequently, CNT-based nanocomposites have been utilized as promising candidates for high-sensitivity strain sensors [13,17,18].

Sensitivity factor is one of the significant indexes of sensitivity analysis for strain sensors [19]. Stable and ultrahigh strain sensitivity is highly desired for high-performance strain sensors [20]. While the steady functional properties of CNCSs have been extensively investigated, corresponding loading-dependent dielectric loss and sensitivity analysis still remain a challenging topic. It is well recognized that the loading-dependent behavior of CNCSs so far have mainly concentrated on the DC strain sensitivity based on the electric resistance. Along this line, Zhang et al. [21] experimentally demonstrated the DC strain sensing functionality of CNT/ polycarbonate nanocomposites through the instantaneous variation of electric resistance. Hu et al. [22] explored both the tensile and compressive DC strain sensitivity of CNT/epoxy nanocomposite sensor. Parmar et al. [23] investigated the influence of CNT nanofiller alignment on the DC strain sensing capability of MWCNT/polycarbonate nanocomposite sensors. Tanabi et al. [24] studied the impact of CNT nanofiller dispersion on the DC strain sensitivity of CNT/epoxy nanocomposite sensor via various mixing speeds and mixing times. In computational simulations, the finite element method (FEM) has been broadly utilized on the current topic. Hu et al. [25] developed a multi-scale three-dimensional (3D) FEM model to predict the piezoresistivity behavior of CNT/ epoxy nanocomposites. Matos et al. [26] developed an FEM model to predict the electromechanical responses of CNCSs in a representative volume element (RVE) with electron tunneling effect and curved configuration of CNT nanofiller. Similarly, Yang et al. [27] extended the numerical research to the piezoresistive response of graphene/rubbery composites based on FEM under the finite deformation framework. In theoretical modelings, several micromechanics-based models have been developed for DC electromechanically coupled behaviors of CNCSs. Xia et al. [28] investigated the strain-dependent electrical resistance and DC strain sensitive capability of CNCSs through the combination of effective-medium approximation (EMA) and Mori-Tanaka (MT) method. Fang et al. [29] explored the piezoresistive modeling of CNCSs under mechanical loadings via an analytic model.

Nevertheless, the DC strain sensitivity factor of CNCSs is often instable under a high strain loading [21,22]. Therefore, the corresponding AC strain sensitivity based on the dielectric loss has attracted increasing attention in experimental observations. In particular, Alamusi et al. [15] explored the influences of AC frequency, strain loading, CNT content, and loading voltage on the dielectric loss of ultrasensitive strain sensor fabricated by MWCNT/epoxy nanocomposite. Zhao et al. [30] investigated the finite strain measurement and AC strain sensing capability of MWCNT/PVDF nanocomposite films manufactured through the solution casting method. Huang et al. [31] studied the synergistic effect of carbon black and MWCNT nanofiller on the AC sensing characteristics of PVDF/HFP nanocomposites. The above experimental results have demonstrated the desirable stability of AC strain sensitivity factor of CNCSs calculated from the dielectric loss. The gap area lies in the fundamental mechanism to connect the microstructural parameter with macroscopic dielectric loss change ratio in the CNT-based nanocomposite sensors.

This paper presents a novel homogenization theory that can quantitatively illustrate the AC electromechanically coupled effects on the dielectric loss and corresponding strain sensing characteristics in CNCSs. It can be used to determine the macroscopic dielectric loss change ratio by choosing a specific CNT volume concentration and AC working frequency, and further significantly simplify the design procedure of highly sensitive strain sensors. This theory not only accounts for the coupled effects between electric and mechanical fields, but also brings in the electric degradation process that leads to the nonlinear coupled characteristics of CNCSs. Several novel features are highlighted as follows:

(i) Dielectric loss change ratio and AC strain sensitivity factor are assessed at a given loading to illustrate the stable AC sensitivity performance of CNCSs;

(ii) Strain loading possesses remarkable impacts on both the hopping function and interfacial thickness. Compared to the field-independent interface effects in the steady environment, various categories of loading-dependent functional interface effects are considered, including strain-affected electron tunneling and hopping [32], Maxwell-Wagner-Sillars (MWS) polarization [33–35], and dielectric relaxation [36] for interfacial permittivity, and imperfect interfacial connection;

(iii) In the development of the electromechanically coupled homogenization scheme under AC loading, the complex conductivity and secant moduli are both employed as the respective homogenization parameters;

(iv) To depict the nonlinear variation of dielectric loss under high strain loading, the evolution equation of electric damage process is established for both the matrix phase and the imperfect interphase.

The remaining sections are organized as follows: Section 2 illustrates the experimental constituents and fabricating procedure of CNCSs. Section 3 presents the electromechanically coupled homogenization method for the dielectric loss change ratio and AC strain sensitivity characteristics of CNCSs. Section 4 calibrates the developed theory with the experiments of MWCNT/PVDF nanocomposite sensor spanning over a broad measuring range. Section 5 provides some conclusive remarks of the study.

2. Experimental studies

Till now, carbon-based nanocomposites have been manufactured through various methods. Poothanari et al. [37] fabricated the MWCNT/polycarbonate (PC)/ polypropylene (PP) nanocomposites through the melt mixing technique. Rezvantalab et al. [38] fabricated the porous MWCNT/PVDF nanocomposites by manipulating the surface energy between the constituent phases. Kaur et al. [39] manufactured the MWCNT/PVDF nanocomposites for the electric energy storage by the vacuum filtration. Basheer et al. [40] presented a review for the fabrication of polymer-grafted CNT nanocomposites. Chikyu et al. [41] fabricated the MWCNT/polyethylene (PE) composite films through a hot-melt method.

The specimen of MWCNT/PVDF nanocomposite sensor was fabricated and measured by Zhao et al. [30]. Note that PVDF polymer ensures a high mechanical strength with remarkable ductility [42]. In addition, PVDF polymer is chemically and thermally stable, which possesses an excellent chemical resistance to corrosion, oxidation and radiation. Therefore, PVDF is an ideal constituent material for fabricating the highly-sensitive strain sensors. In the experiment, the type of CNT nanofiller is MWCNTs-7, which is provided by Nano Carbon Technologies Co., Ltd, Japan. The average diameter and aspect ratio of the MWCNTs are selected as 50 nm and 105, respectively. The type of PVDF matrix is Kynar 740 with the average mass density of 1734 kg/m^3, which is manufactured by Arkema. During the manufacture process of the nanocomposite sensor, the CNTs are dispersed into the solvent with PVDF powder through the ultrasonication process. Then, the nanocomposites are fabricated from the mixture solution via the solution casting method at a constant temperature. Next, the DC and AC electric properties of the nanocomposite specimen are measured during the stretching procedure.

3. Development of the electromechanically coupled homogenization theory

3.1. Preliminaries

To pave the way for the study, first we define the DC and AC strain sensitivity factors, SF_{DC} andSF_{AC}, of CNCSs. Then, the electrical constitutive relations under AC loading and the mechanical ones with plastic deformation in the matrix are described for the CNT and polymer phases, respectively.

3.1.1. DC and AC strain sensitivity factors

Fig. 1 depicts a schematic diagram of the highly sensitive strain sensor manufactured by the CNT-based nanocomposite. This component is adhered to the surface of an object to be tested. The DC electrical resistance and AC dielectric loss of the strain sensor both change in response to the external mechanical loading. The deformation of the object can be measured by the variation of electrical properties in CNCSs. Fig. 2 shows the SEM image of MWCNT/PVDF nanocomposite sensor [30]. Uniformly distributed CNT nanofillers are randomly oriented and located inside the PVDF matrix, forming the agglomeration-free CNT networks in the inlet. Fig. 3 depicts the schematic of electromechanically coupled homogenization for CNCSs subjected to the joint mechanical and AC electrical loadings. Initially, the CNT-based nanocomposite is situated in the undeformed configuration, without strain loading applied to the external boundary. The blue needles represent the randomly distributed CNT nanofillers constituted by one or more layers of cylindrical carbon atoms, while the gray region and a black percolation path denote the polymer matrix and connective CNT networks, respectively. Then, a uniform axial strain loading, ε_x, is applied to the CNCSs along the direction of axis-1. The effective mechanical and functional properties of deformed CNCSs alter gradually in response to the deformation of both CNT nanofillers and polymer matrix.

In order to assess the DC sensitivity performance of CNCSs, the change ratio of electric resistance, $\Delta R_e/R_e$, and DC strain sensitivity factor, SF_{DC}, need to be determined by the relative variation of electric resistance during the gradual deformation process [28]

$$\frac{\Delta R_e}{R_e} = \frac{\chi_e(1+\varepsilon_x)}{\chi_e^{mod}\left(1-\upsilon_e^{mod}\,\varepsilon_x\right)^2} - 1, SF_{DC} = \frac{\Delta R_e}{R_e\varepsilon_x}, \tag{1}$$

where $R_e(=l/\chi_e A)$ and χ_e denote the initial electrical resistance and conductivity of the undeformed CNCS, respectively; l and A are the full-length and cross-section area of CNCSs, respectively; the subscript of "mod" represents the modified properties in the deformed configuration; χ_e^{mod} and v_e^{mod} are the effective conductivity and Poisson ratio of deformed CNCSs, respectively; $\Delta(\cdot)$ defines the variation of the inside quantity during the deformation process.

However, SF_{DC} of CNCSs is not stable under high strain loading. As an alternative, the dielectric loss change ratio,$-\Delta\tan\delta_e/\tan\delta_e$, and AC strain sensitivity factor,SF_{AC}, of CNCSs are defined along a similar route

$$-\frac{\Delta\tan\delta_e}{\tan\delta_e} = 1 - \frac{\chi_e^{mod}\,\phi_e}{\chi_e\phi_e^{mod}}, \quad SF_{AC} = -\frac{\Delta\tan\delta_e}{\tan\delta_e\varepsilon_x}, \tag{2}$$

where $\tan\delta_e(=\chi_e/\omega\phi_e)$ denotes the effective tangent dielectric loss of CNCSs; ϕ_e and ϕ_e^{mod} represent the effective dielectric permittivity of CNCSs in the initial and deformed configurations, respectively; $\omega = 2\pi f$ and f are the angular frequency and AC frequency of external electrical loading, respectively. Note that SF_{AC} is a crucial indicator of sensitivity analysis for strain sensors. The present research will quantitatively determine the effective $-\Delta\tan\delta_e/\tan\delta_e$ and SF_{AC} at a given AC frequency and strain loading to assess the sensitivity performance of CNCSs.

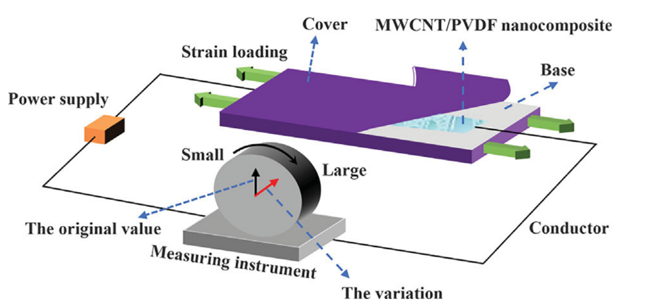

Fig. 1. The schematic diagram of a highly sensitive strain sensor manufactured by CNT-based nanocomposite.

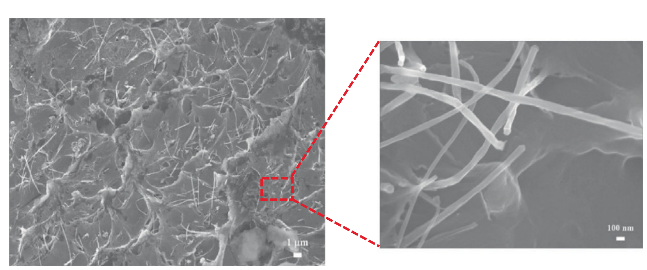

Fig. 2. The SEM image of MWCNT/PVDF nanocomposite sensor. The inlet depicts the connective MWCNT networks. Reprint with permission from Zhao et al., Carbon 129, 585–591 (2018). Copyright 2018 Elsevier Publishing.

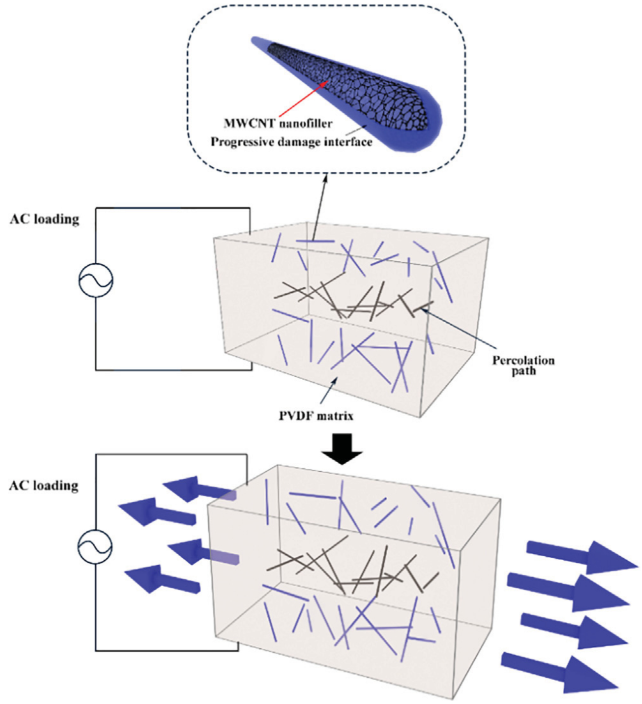

Fig. 3. The schematic of electromechanically coupled homogenization model for CNCSs under tensile loading subjected to AC electrical field.

3.1.2. Electrical constitutive relations of constituent phases

Suppose that the overall CNCSs is subjected to a cyclic electrical loading on the boundary, then the magnitude of current density and electric field can be connected by the complex conductivity

$$\tilde{\mathbf{J}} = \boldsymbol{\chi}^*(\omega)\,\tilde{\mathbf{E}}, \quad \text{with } \boldsymbol{\chi}^*(\omega) = \boldsymbol{\chi} + i\omega\boldsymbol{\phi}, \tag{3}$$

where $\boldsymbol{\chi}^*(\omega)$ denotes the complex conductivity tensor, which is regarded as the electrical homogenization parameter in this electromechanically coupled homogenization model; $\tilde{\mathbf{J}}$ and $\tilde{\mathbf{E}}$ are the amplitudes of the current density and electric field, respectively; i represents the imaginary unit. In the two-phase composite, CNTs will be referred to as phase 1, while the polymer matrix as phase 0, with their respective properties marked by a subscript 1 or 0.

By setting axis-1 as the axial direction and plane 2–3 as the isotropic transverse plane, the complex conductivity tensor of CNTs can be written as

$$\begin{aligned}\boldsymbol{\chi}_1^*(\omega) &=, \mathrm{diag}\chi_1^*(\omega), \chi_3^*(\omega), \chi_3^*(\omega), \quad \text{with } \chi_1^*(\omega)\\ &= \chi_1 + i\omega\phi_1, \quad \chi_3^*(\omega) = \chi_3 + i\omega\phi_3,\end{aligned} \tag{4}$$

where subscripts of "1" and "3" denote the axial and transverse directions of CNTs; χ_1 (or χ_3) and ϕ_1 (or ϕ_3) represent the axial (or transverse) conductivity and permittivity of CNTs, respectively.

Similarly, the complex conductivity of the isotropic polymer matrix at the initial undeformed configuration is given by

$$\boldsymbol{\chi}_0^*(\omega) = \ \mathrm{diag}\{\chi_0^*(\omega), \chi_0^*(\omega), \chi_0^*(\omega)\}, \quad \text{with } \chi_0^*(\omega) = \chi_0 + i\omega\phi_0, \tag{5}$$

where χ_0 and ϕ_0 are the initial conductivity and permittivity of polymer, respectively. In addition, the electric damage is inevitably accumulated in the polymer matrix during the progressive deformation induced by the external mechanical loading. The complex conductivity of the strain-induced electric-damaged matrix is set as

$$\boldsymbol{\chi}_0^{*(D)}(\varepsilon_x, \omega) = \ \mathrm{diag}\{\chi_0^{*(D)}(\varepsilon_x, \omega), \chi_0^{*(D)}(\varepsilon_x, \omega), \chi_0^{*(D)}(\varepsilon_x, \omega)\}, \tag{6}$$

where $\chi_0^{*(D)}(\varepsilon_x, \omega) = \chi_0^{(D)}(\varepsilon_x) + i\omega\phi_0^{(D)}(\varepsilon_x)$; $\chi_0^{(D)}(\varepsilon_x)$ and $\phi_0^{(D)}(\varepsilon_x)$ are the conductivity and permittivity of the electric-damaged matrix

$$\chi_0^{(D)}(\varepsilon_x) = \chi_0(1-\rho_0 D), \quad \phi_0^{(D)}(\varepsilon_x) = \phi_0/(1-\rho_0 D), \quad 0 \leqslant D \leqslant 1, \tag{7}$$

in which ρ_0 is a dimensionless parameter that depicts the maximum electric degradation of the matrix; D is the strain-induced electric damage parameter, which will be determined in Section 3.4. With the evolution of electric damage process, the electric conductivity of matrix phase will decrease, while the corresponding dielectric permittivity will increase instead.

3.1.3. Mechanical constitutive relation of constituent phases

Besides the functional constitutive relations, the mechanical constitutive relations also need to be specified for the constituent phases. First, the linear elastic constitutive relation is adopted for the transversely isotropic CNTs

$$\begin{aligned}&(\sigma_{22}^{(1)} + \sigma_{33}^{(1)}) = 2k_1(\varepsilon_{22}^{(1)} + \varepsilon_{33}^{(1)}) + 2l_1'\varepsilon_{11}^{(1)},\\ &\sigma_{11}^{(1)} = l_1(\varepsilon_{22}^{(1)} + \varepsilon_{33}^{(1)}) + n_1\varepsilon_{11}^{(1)},\\ &(\sigma_{22}^{(1)} - \sigma_{33}^{(1)}) = 2m_1(\varepsilon_{22}^{(1)} - \varepsilon_{33}^{(1)}),\\ &\sigma_{23}^{(1)} = 2m_1\varepsilon_{23}^{(1)}, \quad \sigma_{12}^{(1)} = 2p_1\varepsilon_{12}^{(1)}, \quad \sigma_{13}^{(1)} = 2p_1\varepsilon_{13}^{(1)},\end{aligned} \tag{8}$$

where, in Hill [43] and Walpole [44] notations, k_1, $l_1(l_1' = l_1)$, n_1, m_1 and p_1 are, the plane-strain bulk modulus, cross modulus, axial modulus under an axial strain, transverse shear modulus, and axial shear modulus of CNTs, respectively. It is convenient to rewrite Eq. (8) in their short notations as.

$$\sigma^{(1)} = \mathbf{L}_1\varepsilon^{(1)}, \quad \text{with } \mathbf{L}_1 = (2k_1, l_1, l_1', n_1, 2m_1, 2p_1). \tag{9}$$

Then, the elastoplastic constitutive relation is adopted for the isotropic matrix via the modified Ludwik equation

$$\sigma_e^{(0)} = \sigma_y + h(\varepsilon_e^p)^n, \quad \text{with } \sigma_e^{(0)} = \left(\frac{3}{2}\boldsymbol{\sigma}'^{(0)} : \boldsymbol{\sigma}'^{(0)}\right)^{1/2}, \quad \varepsilon_e^p = \left(\frac{2}{3}\boldsymbol{\varepsilon}_p^{(0)} : \boldsymbol{\varepsilon}_p^{(0)}\right)^{1/2} \tag{10}$$

where σ_y denotes the yield stress, h is the strength index, and n is the strain hardening exponent; $\sigma_e^{(0)}$ denotes the effective von Mises stress, and ε_e^p is the effective plastic strain; $\boldsymbol{\sigma}'^{(0)}$ and $\boldsymbol{\varepsilon}_p^{(0)}$ represent the deviatoric stress tensor and plastic strain tensor, respectively.

A secant-modulus approach is employed by adopting a linear comparison composite to mimic the nonlinear elastoplastic behaviors of the CNCSs [45]. The secant Young's and shear moduli of matrix can be defined after the yielding point

$$E_0^s = \frac{1}{1/E_0 + \varepsilon_e^p/\sigma_e^{(0)}}, \quad \mu_0^s = \frac{3\kappa_0^s E_0^s}{9\kappa_0^s - E_0^s}, \tag{11}$$

where E_0 is the original Young's modulus of matrix, and the superscript of "s" denotes the corresponding secant modulus. The secant bulk modulus of matrix remains unchanged due to the plastic impressibility, i.e. $\kappa_0^s = \kappa_0$. Note that the secant modulus is regarded as the mechanical homogenization parameter of the electromechanically coupled homogenization model.

3.2. Strain- and frequency-dependent functional interface effects between the constituent phases

The external strain loading and AC frequency both possess significant impacts on the functional interface effects between the constituents. Three categories of strain-dependent interface effects need to be considered, including (i) the strain- and filler-dependent electron tunneling and MWS polarization effects, (ii) strain- and frequency-dependent electron hopping and dielectric relaxation effects, (iii) strain-affected imperfect mechanical and electrical connection between the constituents. Here, an ultrathin interphase is considered between the CNTs and polymer matrix to mimic the inevitable flaws and functional interface effects at the interphase [46].

3.2.1. The strain- and filler-dependent functional interface effects

First, the strain loading has remarkable influences on the filler-dependent electron tunneling and MWS polarization via the strain-dependent volume variation of the sensor, the strain-induced electric degradation at the interphase, and the strain-dependent tunneling distance [29]. As the CNT content of CNCSs increases, it increases the probability for the electrons tunneling and charge accumulation at the interphase due to the decreasing average distances between the adjacent CNTs [47]. This variation leads to the formation of the connective CNT networks and nanocapacitors when the CNT content passes through the percolation threshold.

Consequently, the interfacial conductivity and permittivity with strain- and filler-dependent electron tunneling and MWS effects, $\chi_{\text{int}}^{\text{tunneling}}(\varepsilon_x)$ and $\phi_{\text{int}}^{\text{MWS}}(\varepsilon_x)$, can be expressed as

$$\chi_{\text{int}}^{\text{tunneling}}(\varepsilon_x) = \chi_{int}^{(D)}/\tau(c_1^{mod}, c_1^*, \gamma_\chi),$$
$$\phi_{\text{int}}^{\text{MWS}}(\varepsilon_x) = \phi_{int}^{(D)}/\tau(c_1^{mod}, c_1^*, \gamma_\phi), \tag{12}$$

where c_1^{mod} denotes the modified CNT volume concentration of deformed CNCSs

$$c_1^{mod} = \frac{c_1}{(1+\varepsilon_x)(1-v_e^{mod}\,\varepsilon_x)^2}, \tag{13}$$

with c_1 representing the original CNT content in the initial configuration; $\chi_{int}^{(D)}$ and $\phi_{int}^{(D)}$ are, respectively, the conductivity and permittivity of electric-degraded interphase [28]

$$\chi_{int}^{(D)} = \chi_{int}(1-\zeta D), \quad \phi_{int}^{(D)} = \phi_{int}/(1-\zeta D), \tag{14}$$

in which χ_{int} and ϕ_{int} are the initial conductivity and permittivity of the undegraded interphase; ζ is a dimensionless parameter that denotes the maximum electric degradation for the interphase at the complete electric failure state, with $\zeta = \zeta_0 c_1^{-w}$, ζ_0 and w being the CNT resistant parameters for the electric degradation process at the interphase. In addition, $\tau(c_1^{mod}, c_1^*, \gamma)$ is a resistance-like function [48]

$$\tau(c_1^{mod}, c_1^*, \gamma) = \frac{F(1, c_1^*, \gamma) - F(c_1^{mod}, c_1^*, \gamma)}{F(1, c_1^*, \gamma) - F(0, c_1^*, \gamma)}, \quad \text{with}$$
$$F(c_1^{mod}, c_1^*, \gamma) = \frac{1}{\pi}\arctan\left(\frac{c_1^{mod} - c_1^*}{\gamma}\right) + \frac{1}{2}, \tag{15}$$

γ_χ and γ_ϕ denote the scale parameters for electron tunneling of interfacial conductivity and MWS polarization of interfacial permittivity, respectively; c_1^* is the percolation threshold of CNCSs

$$c_1^* = \frac{18 S_{11}^\chi S_{33}^\chi}{-9 S_{11}^\chi 2 + 15 S_{11}^\chi + 2}. \tag{16}$$

Here, S_{11}^χ and S_{33}^χ are the components of Landau depolarization tensor for the electrical field [49]

$$S_{22}^\chi = S_{33}^\chi = \frac{\alpha}{2(\alpha^2-1)^{3/2}}\left[\alpha(\alpha^2-1)^{1/2} - \text{arccosh}\alpha\right],$$
$$S_{11}^\chi = 1 - 2S_{33}^\chi, \quad \alpha > 1, \tag{17}$$

where α is the CNT aspect ratio.

3.2.2. The strain- and frequency-dependent functional interface effects

Then, the strain loading also has obvious impacts on the frequency-dependent electron hopping and dielectric relaxation phenomena via the similar route. The interfacial conductivity and permittivity cannot remain constant as the AC frequency increases. More electrons will hop across the interface at high AC frequency. The strain-dependent average distance between the adjacent CNTs possesses significant influences on the probability of electron hopping. Here, a strain-dependent hopping function, $p(\varepsilon_x, \omega)$, is employed to reveal the strain- and frequency-dependent electron hopping effects

$$p(\varepsilon_x, \omega) = q(\varepsilon_x) \cdot \frac{\omega t_\chi \arctan\omega t_\chi}{\left[0.5\text{Ln}\left(1+\omega^2 t_\chi^2\right)\right]^2 + (\arctan\omega t_\chi)^2}, \quad \text{with}$$
$$q(\varepsilon_x) = \frac{1}{1 + a_{hop} c_1^{-b_{hop}} \varepsilon_x}, \tag{18}$$

where $p(\varepsilon_x, \omega)$ is modified from the Dyre's hopping function [32]; $q(\varepsilon_x)$ denotes the influence of strain loadings on the electron hopping effect; a_{hop} and b_{hop} are the CNT resistant parameters on strain-dependent electron hopping; t_χ is the characteristic time of strain-dependent electron hopping. The interfacial conductivity with the strain- and frequency-dependent electron hopping effects, $\chi_{\text{int}}^{\text{freq}}(\varepsilon_x, \omega)$, is now represented via

$$\chi_{\text{int}}^{\text{freq}}(\varepsilon_x, \omega) = \chi_{\text{int}}^{\text{tunneling}}(\varepsilon_x) \cdot p(\varepsilon_x, \omega). \tag{19}$$

Similarly, the electrons accumulated at the interphase decrease in regard to the AC frequency, which can be ascribed as the dielectric relaxation effect. The strain loading will influence this effect via the electric-degraded interphase and the updated CNT volume concentration. The impact of strain- and frequency-dependent Debye's dielectric relaxation effect is obtained as [36]

$$\phi_{\text{int}}^{\text{freq}}(\varepsilon_x, \omega) = \left(\phi_{int}^{\text{inf}}(\varepsilon_x) + \frac{\phi_{int}^{\text{MWS}}(\varepsilon_x) - \phi_{int}^{\text{inf}}(\varepsilon_x)}{1+\omega^2 t_\phi^2}\right), \quad \text{with}$$
$$\phi_{int}^{\text{inf}}(\varepsilon_x) = \phi_{\text{int}(0)}^{\text{inf}(D)}/\tau(c_1^{mod}, c_1^*, \gamma_{\text{inf}}^\phi), \tag{20}$$

where $\phi_{int}^{\text{inf}}(\varepsilon_x)$ is the strain-dependent dielectric permittivity of interphase with MWS polarization at $f = \infty$; t_ϕ is the characteristic time of strain-dependent dielectric relaxation; $\phi_{int(0)}^{\text{inf}(D)}$ $(= \phi_{int(0)}^{\text{inf}}/(1-\xi D))$ and $\phi_{int(0)}^{\text{inf}}$ are the degraded and initial permittivity of the interphase at $f = \infty$, respectively; γ_{inf}^ϕ is the scale parameter of MWS polarization at $f = \infty$.

3.2.3. The strain-dependent imperfect mechanical and electrical connection between the constituent phases

Next, the strain loading will influence both mechanical and electrical connection between the adjacent constituents. A strain-dependent interphase thickness, $d(\varepsilon_x)$, is adopted to characterize this strain-affected imperfect connection

$$d(\varepsilon_x) = d_0(1 + a_{int} c_1^{-b_{int}} \varepsilon_x), \tag{21}$$

where d_0 is the initial interfacial thickness; a_{int} and b_{int} represent the CNT influences on the strain-dependent interfacial thickness.

The strain-dependent mechanical and electrical properties of coated CNTs surrounded by an ultrathin interphase can be calculated via the Mori-Tanaka (MT) method

$$\mathbf{L}_c = \mathbf{L}_{int}\left\{\mathbf{I} + (1-c_{int})\left[c_{int}\mathbf{S}_{int}^\sigma + (\mathbf{L}_1 - \mathbf{L}_{int})^{-1}\mathbf{L}_{int}\right]^{-1}\right\}, \tag{22}$$

$$\eta_i^{(c)}(\varepsilon_x, \omega) = \eta_{\text{int}}^{freq}(\varepsilon_x, \omega)\left[1 + \frac{(1-c_{\text{int}})(\eta_i - \eta_{\text{int}}^{freq}(\varepsilon l_x, \omega))}{c_{\text{int}} S_{ii}^\chi(\eta_i - \eta_{\text{int}}^{freq}(\varepsilon_x, \omega)) + \eta_{\text{int}}^{freq}(\varepsilon_x, \omega)}\right],$$
$$\text{with } \eta = \chi \text{ or } \phi, \tag{23}$$

where $\mathbf{L}_c = (2k_c, l_c, l_c', n_c, 2m_c, 2p_c)$ and $\mathbf{L}_{int} = (2k_{int}, l_{int}, l_{int}', n_{int}, 2m_{int}, 2p_{int})$ denote the elastic stiffnesses of the coated CNTs and interphase, respectively; $\mathbf{I}$ is the unit tensor; $\mathbf{S}_{int}^{\sigma}$ and S_{ii}^{χ} are the Eshelby S-tensor for the mechanical field and Landau depolarization tensor for the electric field, respectively; c_{int} represents the strain-dependent interphase volume concentration in the coated nanofiller

$$c_{int} = 1 - \frac{L \cdot (L/\alpha)^2}{[L + d(\varepsilon_x)] \cdot [L/\alpha + d(\varepsilon_x)]^2}, \tag{24}$$

in which L is the half-length of CNT nanofiller. The complex conductivity of coated CNTs with the stated strain- and frequency-dependent interface effects is calculated by $\chi_i^{(c)*}(\varepsilon_x, \omega) = \chi_i^{(c)}(\varepsilon_x, \omega) + i\omega\phi_i^{(c)}(\varepsilon_x, \omega)$, with $i = 1$ and 3 denoting the axial and transverse directions, respectively.

3.3. Electromechanically coupled homogenization scheme of CNT-polymer nanocomposite sensor

3.3.1. The functional homogenization scheme of CNCSs

An electromechanically coupled homogenization scheme will be developed for CNCSs via a joint effective-medium approximation (EMA) and Mori-Tanaka (MT) method. The strain-and frequency-dependent complex conductivity, secant moduli, and dielectric loss of CNCSs are then calculated at a specific loading. It directly connects the microstructural parameters such as CNT content and aspect ratio with the effective AC sensitivity performance of CNCSs.

In the homogenization of electric field, the strain-dependent complex conductivity of CNCSs,$\chi_e^{*\ mod}(\varepsilon_x, \omega)$, can be revealed via the EMA at a given strain loading and AC frequency [48,50]

$$\begin{aligned}
&(1 - c_1^{mod})\frac{\chi_0^{(D)*}(\varepsilon_x,\omega) - \chi_e^{*\ mod}(\varepsilon_x,\omega)}{\chi_e^{*\ mod}(\varepsilon_x,\omega) + (1/3)\left(\chi_0^{(D)*}(\varepsilon_x,\omega) - \chi_e^{*\ mod}(\varepsilon_x,\omega)\right)} \\
&\quad + \frac{1}{3}c_1^{mod}\left[\frac{2\left(\chi_3^{(c)*}(\varepsilon_x,\omega) - \chi_e^{*\ mod}(\varepsilon_x,\omega)\right)}{\chi_e^{*\ mod}(\varepsilon_x,\omega) + S_{33}^{\chi}\left(\chi_3^{(c)*}(\varepsilon_x,\omega) - \chi_e^{*\ mod}(\varepsilon_x,\omega)\right)}\right. \\
&\quad \left. + \frac{\chi_1^{(c)*}(\varepsilon_x,\omega) - \chi_e^{*\ mod}(\varepsilon_x,\omega)}{\chi_e^{*\ mod}(\varepsilon_x,\omega) + S_{11}^{\chi}\left(\chi_1^{(c)*}(\varepsilon_x,\omega) - \chi_e^{*\ mod}(\varepsilon_x,\omega)\right)}\right] = 0,
\end{aligned} \tag{25}$$

where $\chi_0^{(D)*}(\varepsilon_x, \omega)$ is the complex electric conductivity of the electric-degraded matrix; $\chi_1^{(c)*}(\varepsilon_x, \omega)$ (or $\chi_3^{(c)*}(\varepsilon_x, \omega)$) are the axial (or transverse) complex conductivity of coated CNTs with stated interface effects. The effective conductivity, permittivity and dielectric loss of CNCSs can be obtained from the components of $\chi_e^{*\ mod}(\varepsilon_x, \omega)$.

3.3.2. The mechanical homogenization scheme of CNCSs

In the homogenization of mechanical field, the strain-dependent secant bulk and shear moduli of the CNCSs, κ_s^{mod} and μ_s^{mod}, can be calculated via the MT method at a given strain loading [51]

$$\begin{aligned}
\kappa_s^{mod} &= \frac{(1 - c_1^{mod})\kappa_0^s + c_1^{mod}\xi_s^{LA}}{(1 - c_1^{mod}) + 3c_1^{mod}\xi_s^{A}}, \\
\mu_s^{mod} &= \frac{(1 - c_1^{mod})\mu_0^s + c_1^{mod}\eta_s^{LA}}{(1 - c_1^{mod}) + 2c_1^{mod}\eta_s^{A}},
\end{aligned} \tag{26}$$

where ξ_s^{LA}, ξ_s^{A}, η_s^{LA} and η_s^{A} are parameters of mechanical homogenization model, which are listed in Appendix A in the Supplementary Information (SI). This scheme applies to randomly oriented transversely isotropic CNT nanofillers homogeneously dispersed in the isotropic polymer matrix.

In addition, the effective stresses in the matrix phase need to be determined. A convenient way lies in the field-fluctuation method [52]. When subjected to a fixed external loading, a variation of one constituent mechanical parameter will lead to a field fluctuation that gives rise to a new overall elastic energy. By taking μ_0^s and κ_0^s as the constituent parameters to vary separately, the effective Mises and bulk stresses of the matrix phase can be obtained at a fixed external loading

$$\sigma_e^{(0)} = \left\{\frac{1}{(1 - c_1^{mod})}\left[\left(\frac{\mu_0^s}{\kappa_s^{mod}}\right)^2 \frac{\partial \kappa_s^{mod}}{\partial \mu_0^s}\frac{\bar{\sigma}_{kk}^2}{3} + \left(\frac{\mu_0^s}{\mu_s^{mod}}\right)^2 \frac{\partial \mu_s^{mod}}{\partial \mu_0^s}\bar{\sigma}_e^2\right]\right\}^{\frac{1}{2}}, \tag{27}$$

$$\sigma_{kk}^{(0)} = \left\{\frac{1}{(1 - c_1^{mod})}\left[\left(\frac{\kappa_0^s}{\kappa_s^{mod}}\right)^2 \frac{\partial \kappa_s^{mod}}{\partial \kappa_0^s}\bar{\sigma}_{kk}^2 + 3\left(\frac{\kappa_0^s}{\mu_s^{mod}}\right)^2 \frac{\partial \mu_s^{mod}}{\partial \kappa_0^s}\bar{\sigma}_e^2\right]\right\}^{\frac{1}{2}}, \tag{28}$$

where $\bar{\sigma}_e = \sqrt{\frac{3}{2}\bar{\boldsymbol{\sigma}}' : \bar{\boldsymbol{\sigma}}'}$ and $\bar{\sigma}_{kk} = \mathrm{tr}(\bar{\boldsymbol{\sigma}})$ are the external effective Mises stress and bulk stress applied to the nanocomposites, with $\bar{\boldsymbol{\sigma}}$ denoting the external mechanical loading.

3.4. Thermodynamics of electric damage process in the matrix phase

As the external mechanical loading increases, the electric damage will accumulate in the matrix phase. It will lower its electrical conductivity but enhance its dielectric permittivity. The evolution of electric damage can be depicted by the principle of irreversible thermodynamics

$$\begin{aligned}
&-\left.\frac{\partial \psi_e^{(0)}}{\partial D}\right|_{\sigma} dD \geqslant 0, \quad \text{with} \\
&\psi_e^{(0)} = \frac{1}{2}(1 - D)\left[\frac{2(1 + \nu_0)}{3E_0}\sigma_e^{(0)2} + \frac{(1 - 2\nu_0)}{3E_0}\sigma_{kk}^{(0)2}\right],
\end{aligned} \tag{29}$$

where $\psi_e^{(0)}$ denotes the elastic stored energy of matrix phase. The corresponding thermodynamic driving force of electric damage process, f_{driv}^{D}, can be defined as a negative derivative of elastic stored energy density in regard to the electric damage parameter at a generic state

$$f_{driv}^{D} = -\left.\frac{\partial \psi_e}{\partial D}\right|_{\sigma} = \frac{1}{2}\left[\frac{2(1 + \nu_0)}{3E_0}\sigma_e^{(0)2} + \frac{(1 - 2\nu_0)}{3E_0}\sigma_{kk}^{(0)2}\right]. \tag{30}$$

The electric damage process starts to evolve and accumulate in the matrix phase when the effective stress reaches the threshold value. A Landau-Ginsburg-like equation is derived to describe the evolution of the electric damage process

$$\frac{\mathrm{d}D}{\mathrm{d}\varepsilon_e^p} = \begin{cases} 0, & \sigma_e^{(0)} \leqslant \sigma_{cr} \\ Q(D, \varepsilon_e^p) \cdot f_{driv}^{D}, & \sigma_e^{(0)} > \sigma_{cr} \end{cases}, \quad \text{with } Q(D, \varepsilon_e^p) = \frac{(1 - D)^m}{S_0 (\varepsilon_e^p)^s}, \tag{31}$$

where m and s are electric damage exponents of the polymer; S_0 is the electric energy strength; σ_{cr} is the threshold stress of electric damage. The electric failure will take place when D finally reaches 1. Very recently, a similar evolution equation has been utilized to govern the dielectric breakdown process in graphene-based nanocomposites [53].

At this stage, the electromechanically coupled homogenization model for the dielectric loss change ratio and AC strain sensitivity factor of CNT-based nanocomposite sensors has been completely established. Recognizing that $\tan\delta_e = \chi_e/\omega\phi_e$, the ratio of effective permittivity to effective conductivity of the nanocomposite, the two critical factors, $-\Delta\tan\delta_e/\tan\delta_e$ and SF_{AC}, now can be determined accordingly to assess the sensitivity performance of CNCSs.

4. Model calibrations and discussion

4.1. Computational procedures

This electromechanically coupled model will be calibrated via the direct comparison with the experiments of MWCNT/PVDF nanocomposite sensor in this section [30]. The axial and transverse electric properties of CNTs are $\chi_1 = 8.9 \times 10^2 \mathrm{S/m}$, $\phi_1 = 15\phi_{vac}$, $\chi_3 (= \chi_2) = 10^{-3}\chi_1$, $\phi_3 (= \phi_2) = 10\phi_{vac}$, with $\phi_{vac} = 8.85 \times 10^{-12} \mathrm{F/m}$ denoting the permittivity in the vacuum, while the corresponding mechanical properties are $E_{11} = 1.06$ TPa, $v_{12} = 0.162$, $\kappa_{23} = 271$ GPa, $\mu_{12} = 442$ GPa and $\mu_{23} = 17$ GPa. The weight percentage in the experiments are converted into volume concentration by setting the MWCNT and PVDF mass densities as 2100 kg/m^3 and 1734 kg/m^3, respectively. Other material properties of constituents and interface effects are listed in Table S1-S2 in the SI, respectively.

Fig. S1 in the SI depicts the flowchart of electromechanically coupled homogenization model to assess the dielectric loss change ratio and strain sensitivity factor of CNCSs. The computational scheme can be divided into the mechanical and electrical parts. First, the mechanical homogenization scheme is performed under a given strain loading. The effective secant moduli of CNCSs are calculated via the MT method in Eq. (26). c_1^{mod} is updated from Eq. (13) under the deformed configuration. The electric damage parameter,D, can be determined by the evolution equation of electric damage in Eq. (31). Then, the homogenization evaluation is conducted in the electric field under a given AC frequency. The electric properties of coated CNT nanofillers are obtained with strain- and frequency-dependent functional and mechanical interface effects in Eqs. (12)-(23). The effective complex conductivity of CNCSs is calculated via the EMA from Eq. (25) under the initial and deformed configurations, respectively. $-\Delta\tan\delta_e/\tan\delta_e$ and SF_{AC} of CNCSs are finally evaluated by Eq. (2). Next, another strain step is imposed on the boundary of CNCSs until the strain loading meets the requirement.

4.2. Model verification under DC condition

First, the present electromechanically coupled homogenization model of CNCSs is verified under DC condition. Fig. 4(a) shows the effective electric resistance change ratio, $\Delta R_e/R_e$, of CNCSs in regard to the axial strain. The theoretical prediction of $\Delta R_e/R_e$ is consistent with the experiments of Zhao et al. [30], spanning over the strain range from 0 to 10% at all three selected CNT volume concentrations, i.e. 0.496%, 0.661% and 0.827%. Note that $\Delta R_e/R_e$ increases linearly with the axial strain at the low strain range, while it starts to enhance significantly when the strain loading approximately reaches 2%. It can be explained by the electric damage process when the effective stress in the matrix exceeds a certain value. In addition, the effective electric resistance change ratio decreases in regard to the CNT volume concentration. This decreasing trend on the resistance change ratio was also validated in MWCNT/epoxy nanocomposites by Yin et al. [54]. Consequently, the present electromechanically coupled homogenization model of CNCSs has been validated under DC electric condition.

Fig. 4(b) analyzes the effective SF_{DC} of CNCSs in regard to the axial strain. It is shown that SF_{DC} under low CNT loading increases remarkably when ε_x exceeds 2%. In addition, SF_{DC} decreases with the addition of CNTs, due to the decreasing $\Delta R_e/R_e$ as shown in Fig. 4(a). A similar trend on the effective SF_{DC} was reported in CNT/epoxy nanocomposites by Hu et al. [22]. This phenomenon confirms the drawbacks of adopting $\Delta R_e/R_e$ as the measuring parameter of CNCSs that corresponding sensitivity factor, SF_{DC}, cannot hold constant under a high strain loading.

4.3. Strain- and frequency-dependent dielectric loss change ratio under AC electrical loading

Then, we investigate the strain- and frequency-dependent dielectric loss, $\tan\delta_e$, and corresponding change ratio, $-\Delta\tan\delta_e/\tan\delta_e$, of CNCSs. Fig. 5(a) depicts the effective dielectric loss of CNCSs in regard to the CNT loading under various interface conditions at 100 kHz and $\varepsilon_x = 0$. Three categories of interface conditions are investigated. First, the calculation is conducted under the perfect interface condition in the green line. The dielectric loss increases significantly when the c_1 passes through the percolation threshold. However, the magnitude of $\tan\delta_e$ reaches 10^4, which exceeds the order of magnitudes from CNCSs [55]. It implies the existence of imperfect interphase between the constituents. The dielectric loss considering the imperfect interface connection decreases remarkably to 10^{-2}, as shown by the blue line. It is much lower than the experimental facts. After considering the filler- and frequency-dependent interface effects, the effective $\tan\delta_e$ increases after reaching the percolation threshold, as shown by the red line. The effective dielectric loss of CNCSs enhances with the CNT volume concentration. The magnitude of dielectric loss is close to 10^2, which agrees with the magnitude of experimental data [55]. Fig. 5(b) shows the effective $\tan\delta_e$ in regard to the AC frequency under different CNT contents. Both filler- and frequency-dependent interface effects have been included. As the AC frequency increases, the dielectric polarization at the interface decreases. Consequently, the corresponding dielectric loss also

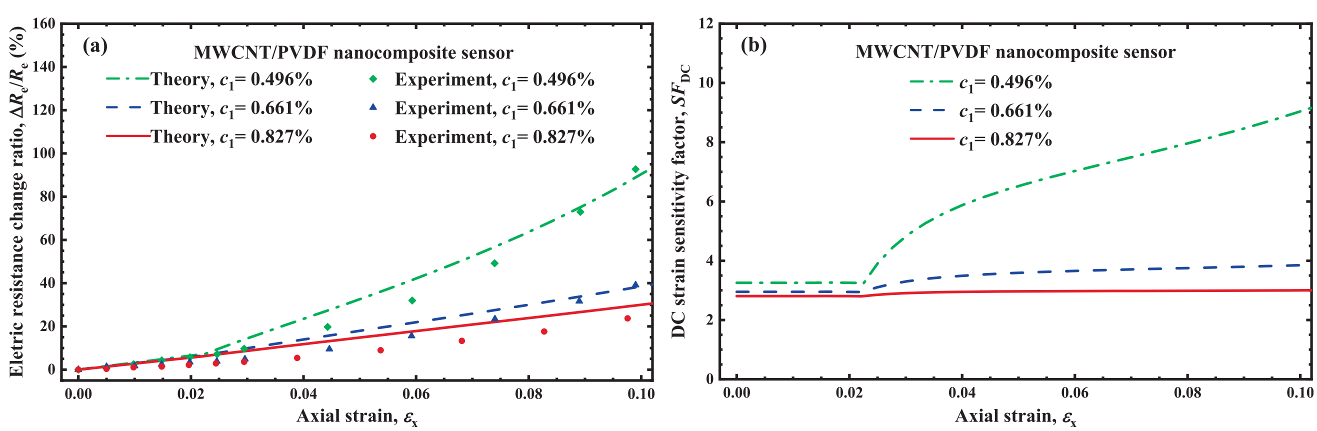

Fig. 4. (a) The electric resistance change ratio and (b) DC strain sensitivity factor of MWCNT/PVDF nanocomposite sensor in regard to axial strain.

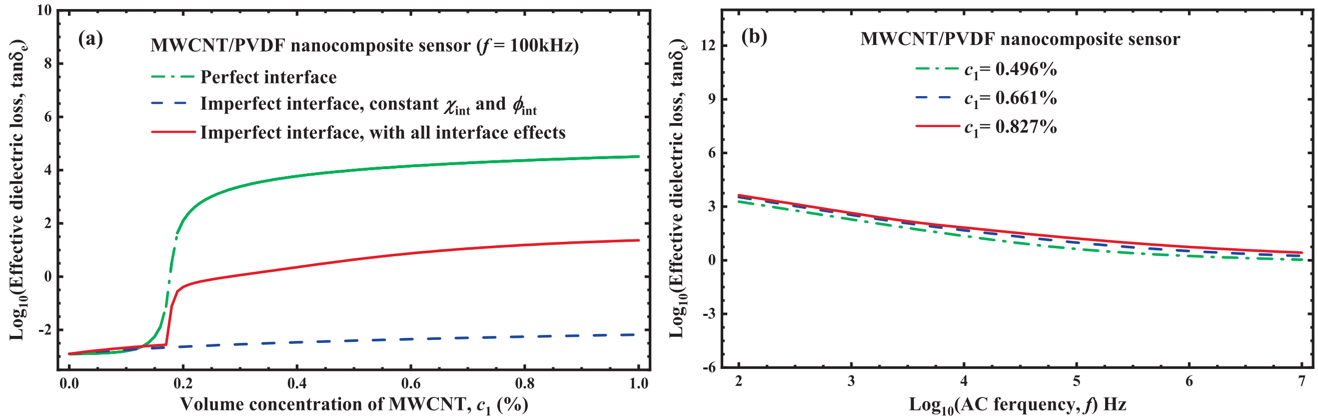

Fig. 5. The effective dielectric loss of MWCNT/PVDF nanocomposite sensor in regard to (a) CNT loading under different interface conditions, (b) AC frequency under various CNT loadings.

decreases with the AC frequency, which is consistent with the experimental trend of Yadav et al. [55].

Fig. 6(a)-6(b) reveal the dielectric loss change ratio of CNCSs in regard to axial strain under various CNT contents. Under both 100 kHz and 500 kHz, the theoretical predictions of $-\Delta\tan\delta_e/\tan\delta_e$ are consistent with the experimental data [30] at the selected CNT volume concentrations spanning over the whole measuring strain from 0 to 10%. In the low strain range, $-\Delta\tan\delta_e/\tan\delta_e$ increases slowly with the axial strain. It can be explained by the variation of modified CNT volume concentration, c_1^{mod}, under the deformed configuration. In addition, the dielectric loss change ratio decreases with the increase of the CNT volume

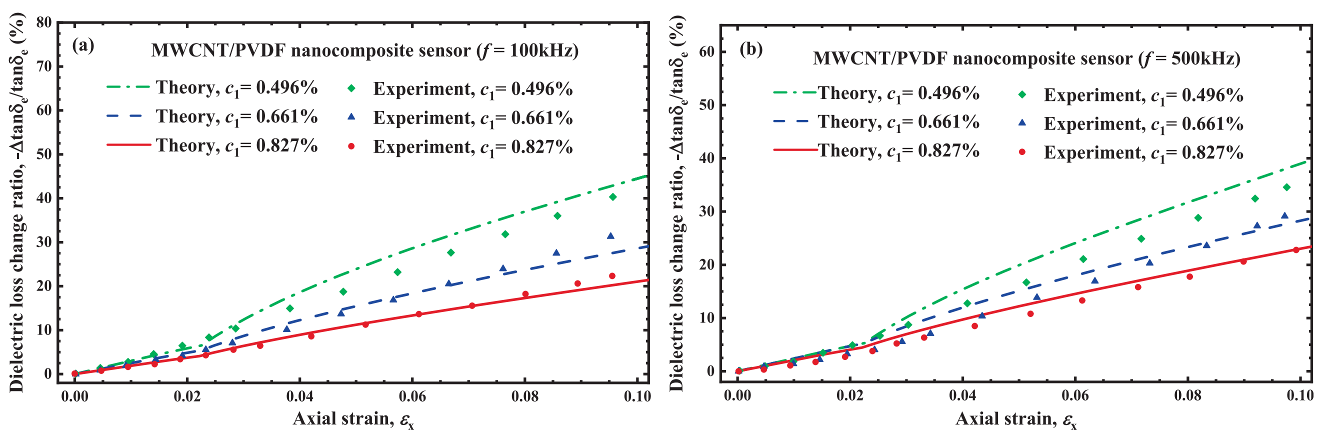

Fig. 6. The dielectric loss change ratio of MWCNT/PVDF nanocomposite sensor in regard to the axial strain under (a) 100 kHz and (b) 500 kHz.

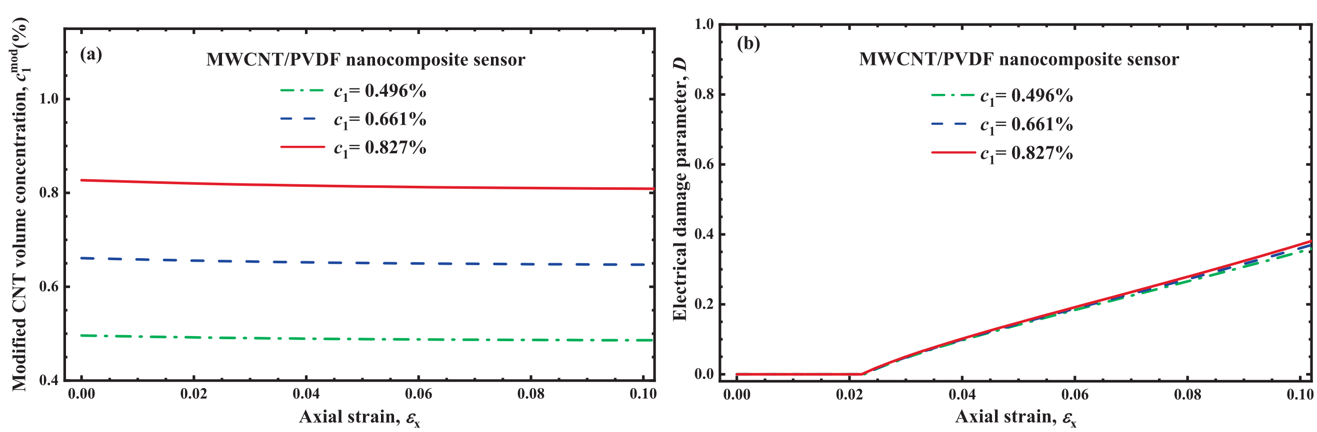

Fig. 7. (a) The modified CNT volume concentration and (b) the electric damage parameter of MWCNT/PVDF nanocomposite sensor in regard to the axial strain under different CNT loadings.

concentration, c_1. Fig. 7(a) shows that c_1^{mod} decreases in regard to the axial strain. However, $-\Delta\tan\delta_e/\tan\delta_e$ enhances significantly with the axial strain when the strain loading increases to a certain extent. The underlying reason can be revealed by the evolution of electric damage process as depicted in Fig. 7(b). The electric damage process starts to accumulate in the matrix phase and interphase when the matrix stress reaches the threshold value. In addition, Fig. 8 reveals that $-\Delta\tan\delta_e/\tan\delta_e$ of CNCSs decreases in regard to the CNT content. A similar trend on the $-\Delta\tan\delta_e/\tan\delta_e$ was reported in MWCNT/epoxy nanocomposites by Tong et al. [56]. This trend can be explained by the variation of c_1-dependent dielectric loss in the inlet of Fig. 8. As CNT volume concentrations increases, $\tan\delta_e$ enhances remarkably, while $-\Delta\tan\delta_e$ merely increases smoothly.

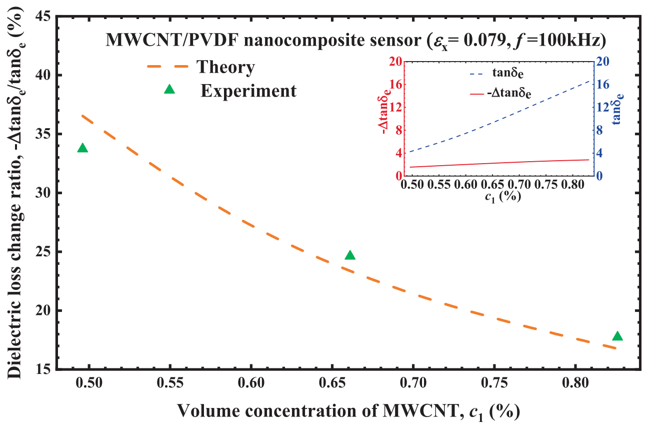

Fig. 8. The dielectric loss change ratio of MWCNT/PVDF nanocomposite sensor in regard to CNT volume concentration. The inlet depicts the impacts of CNT volume concentration on the $\tan\delta_e$ and $-\Delta\tan\delta_e$, respectively.

Fig. 9(a) shows the influences of AC frequency on the dielectric loss change ratio of CNCSs. The theoretical predictions of dielectric loss change ratio are calibrated with the experimental data under different AC frequencies among the whole strain range from 0 to 10% [30]. It is revealed that the dielectric loss change ratio decreases in regard to the AC frequency, as shown in Fig. 9(b). To explain this phenomenon, we plot the inlet of Fig. 9(b) to reveal that $\tan\delta_e$ goes down significantly as AC frequency increases, while $-\Delta\tan\delta_e$ only decreases smoothly.

4.4. AC strain sensitivity factor of CNCSs

Next, we quantitatively assess the strain- and frequency-dependent AC strain sensitivity factor, SF_{AC}, of CNCSs. Fig. 10(a) shows that SF_{AC} of CNCSs nearly keeps constant in regard to the axial strain under various CNT loadings. In addition, SF_{AC} decreases with the CNT volume concentration, which is similar to the trend of DC strain sensitivity factor [28]. Fig. 10(b) reveals that SF_{AC} of

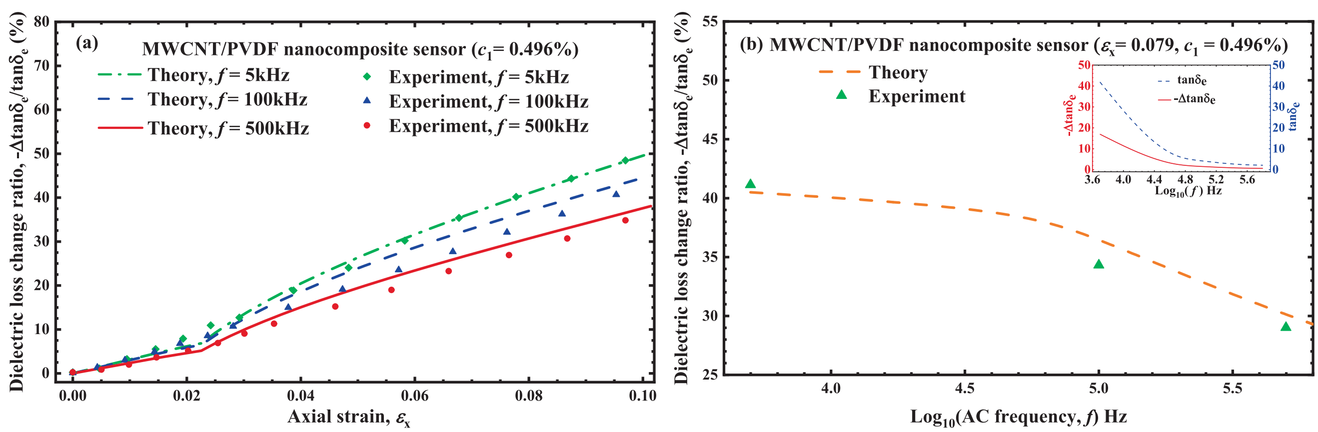

Fig. 9. The dielectric loss change ratio of MWCNT/PVDF nanocomposite sensor in regard to (a) the axial strain under different AC frequencies, (b) AC frequency. The inlet of Fig. 9(b) shows the influences of AC frequency on the $\tan\delta_e$ and $-\Delta\tan\delta_e$, respectively.

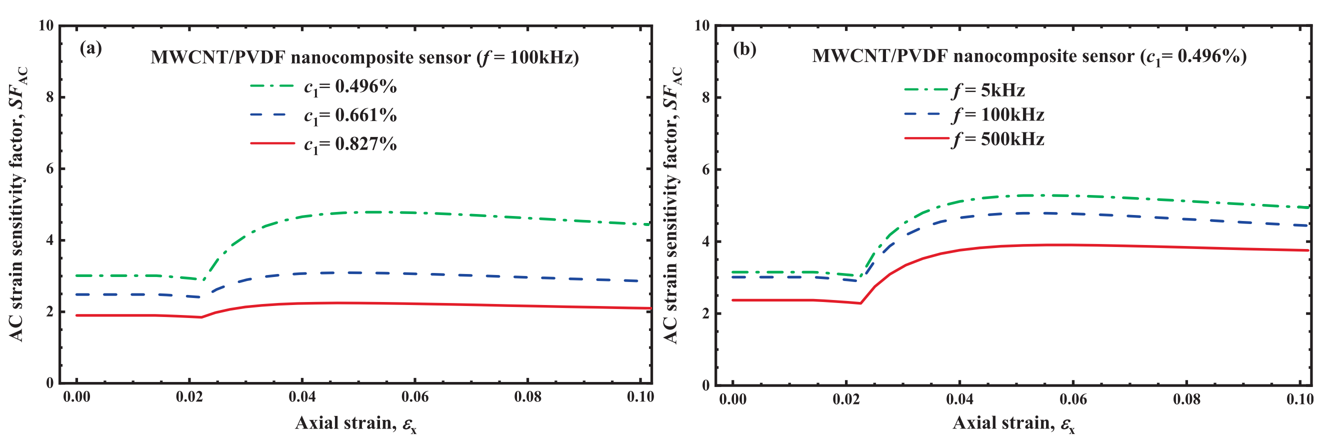

Fig. 10. The AC strain sensitivity factor of MWCNT/PVDF nanocomposite sensor in regard to the axial strain under various (a) CNT loadings and (b) AC frequencies.

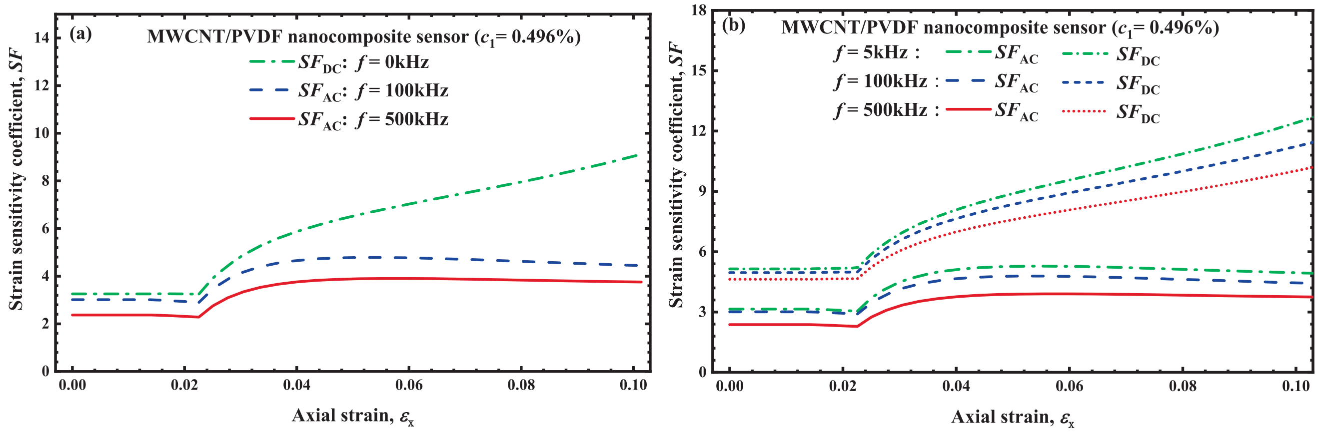

Fig. 11. (a) The comparison of SF_{DC} and SF_{AC} of MWCNT/PVDF nanocomposite sensor in regard to the axial strain, (b) the comparison of SF_{AC} and SF_{DC} of MWCNT/PVDF nanocomposite sensor in regard to the axial strain under different AC frequencies.

CNCSs decreases with the AC frequency due to the decreasing dielectric loss change ratio under the identical strain loading.

4.5. Comparison of DC and AC strain sensitivity factors for CNCSs

Fig. 11(a) depicts that SF_{DC} under the DC condition is higher than SF_{AC} under AC condition, but SF_{AC} is more stable than SF_{DC} over the whole strain loading range. In addition, Fig. 11(b) depicts the comparison between the DC and AC strain sensitivity factors of CNCSs under different AC frequencies. Under the AC loading, SF_{AC} is still more stable than SF_{DC} over the whole strain loading range. It confirms the advantage on demarcating CNCSs via the dielectric loss over the traditional electric resistance in both DC and AC conditions.

5. Conclusions

In this work, we have developed an electromechanically coupled homogenization model to quantitatively illustrate the combined effects of mechanical loading and AC frequency on the dielectric loss change ratio and the strain sensitivity characteristics of CNCSs. First, the complex conductivity and secant moduli are both employed as the homogenization parameters of this electromechanically coupled theory with joint effective-medium approximation and Mori-Tanaka method. Then, various categories of loading-dependent functional interface effects are considered through the strain-dependent hopping function and interfacial thickness. Finally, the evolution of electric damage process is characterized by irreversible thermodynamics.

The theoretical predictions of AC dielectric loss change ratio are calibrated with the experiments of MWCNT/PVDF nanocomposite sensor over a broad strain range from 0 to 10% and a wide frequency spectrum from 5 kHz to 500 kHz. It is revealed that the AC strain sensitivity factor of CNCSs is able to nearly keep constant with external strain loading, while the dielectric loss change ratio decreases with both CNT volume concentration and AC frequency. The present study confirms the advantage on demarcating CNCSs via the dielectric loss over the electric resistance.

This research establishes a direct connection between the microstructural parameters and dielectric loss change ratio of CNT-based nanocomposite sensor. It can be used to rapidly determine the macroscopic dielectric loss change ratio by choosing a specific CNT volume concentration and AC working frequency, and further simplify the design procedure of highly sensitive strain sensors.

Declaration of Competing Interest

The authors declare that they have no known competing financial interests or personal relationships that could have appeared to influence the work reported in this paper.

Acknowledgements

X.D. Xia acknowledges the support form National Natural Science Foundation of China (Grant No. 11902365) and Natural Science Foundation of Hunan Province (Grant No. 2020JJ5685). H.M. Yin acknowledges the support from National Science Foundation (Grant No. CMMI-1762891). G.J. Weng acknowledges the support from NSF Mechanics of Materials and Structures Program (Grant No. CMMI-1162431).

Data availability

The raw/processed data required to reproduce these findings cannot be shared at this time as the data also forms part of an ongoing study.

Appendix A. Supplementary material

Supplementary data to this article can be found online at https://doi.org/10.1016/j.matdes.2022.110557.

References

[1] Y. Liu, H. Zheng, M. Liu, High performance strain sensors based on chitosan/carbon black composite sponges, Mater. Design 141 (2018) 276–285.
[2] M.S. Cetin, H.A.K. Toprakci, Flexible electronics from hybrid nanocomposites and their application as piezoresistive strain sensors, Compos. Part B - Eng. 224 (2021) 109199.
[3] C. Zhao, Z. Xia, X. Wang, J. Nie, P. Huang, S. Zhao, 3D-printed highly stable flexible strain sensor based on silver-coated-glass fiber-filled conductive silicon rubber, Mater. Design 193 (2020) 108788.
[4] F. Marra, S. Minutillo, A. Tamburrano, M.S. Sarto, Production and characterization of graphene nanoplatelet-based ink for smart textile strain sensors via screen printing technique, Mater. Design 198 (2021) 109306.
[5] J. Britton, K. Krukiewicz, M. Chandran, J. Fernandez, A. Poudel, J.-R. Sarasua, U. FitzGerald, M.J. Biggs, A flexible strain-responsive sensor fabricated from a biocompatible electronic ink via an additive-manufacturing process, Mater. Design 206 (2021) 109700.
[6] Y. Li, X. Miao, J.Y. Chen, G. Jiang, Q. Liu, Sensing performance of knitted strain sensor on two-dimensional and three-dimensional surfaces, Mater. Design 197 (2021) 109273.
[7] H. Wang, X. Ma, Y. Hao, Electronic devices for human-machine interfaces, Adv. Mater. Interfaces 4 (4) (2017) 1600709, https://doi.org/10.1002/admi.201600709.

[8] L. Vertuccio, L. Guadagno, G. Spinelli, P. Lamberti, V. Tucci, S. Russo, Piezoresistive properties of resin reinforced with carbon nanotubes for health-monitoring of aircraft primary structures, Compos. Part B - Eng. 107 (2016) 192–202.
[9] H. Yao, W. Yang, W. Cheng, Y.J. Tan, H.H. See, S.i. Li, H.P.A. Ali, B.Z.H. Lim, Z. Liu, B.C.K. Tee, Near–hysteresis-free soft tactile electronic skins for wearables and reliable machine learning, Proc. Natl. Acad. Sci. 117 (41) (2020) 25352–25359.
[10] M.J. Yee, N. Mubarak, E. Abdullah, M. Khalid, R. Walvekar, R.R. Karri, S. Nizamuddin, A. Numan, Carbon nanomaterials based films for strain sensing application—A review, Nano-Struct. Nano-Objects 18 (2019) 100312.
[11] Q. Zhao, L. Yang, Y. Ma, H. Huang, H. He, H. Ji, Z. Wang, J. Qiu, Highly sensitive, reliable and flexible pressure sensor based on piezoelectric PVDF hybrid film using MXene nanosheet reinforcement, J. Alloys Compd. 886 (2021) 161069.
[12] S. Carter, A. Ned, J. Chivers, A. Bemis, Selecting piezoresistive vs. piezoelectric pressure transducers, *Kulite Semiconductor Products*, Inc (2016) 1–25.
[13] S.H. Jang, H.M. Yin, Effect of aligned ferromagnetic particles on strain sensitivity of multi-walled carbon nanotube/polydimethylsiloxane sensors, Appl. Phys. Lett. 106 (2015) 141903.
[14] J. Abraham, K. Sidhardhan Sisanth, A.K. Zachariah, H.J. Mariya, S.C. George, N. Kalarikkal, S. Thomas, Transport and solvent sensing characteristics of styrene butadiene rubber nanocomposites containing imidazolium ionic liquid modified carbon nanotubes, J. Appl. Polym. Sci. 137 (2020) 49429.
[15] W.F.Y. Alamusi, Y. Surina, N. Li, H.M. Hu, Y.L. Ning, L.K. Liu, S. Wu, H.F. Atobe, Ultrasensitive strain sensors of multiwalled carbon nanotube/epoxy nanocomposite using dielectric loss tangent, Appl. Phys. Lett. 103 (2013) 221903.
[16] Q. Cheng, B. Wang, C. Zhang, Z. Liang, Functionalized carbon-nanotube sheet/bismaleimide nanocomposites: mechanical and electrical performance beyond carbon-fiber composites, Small 6 (2010) 763–767.
[17] X. Wan, F. Zhang, Y. Liu, J. Leng, CNT-based electro-responsive shape memory functionalized 3D printed nanocomposites for liquid sensors, Carbon 155 (2019) 77–87.
[18] S.H. Jang, H.M. Yin, Effective electrical conductivity of carbon nanotube-polymer composites: a simplified model and its validation, Mater. Res. Express 2 (2015) 045602.
[19] T. Yan, Z. Wang, Y.-Q. Wang, Z.-J. Pan, Carbon/graphene composite nanofiber yarns for highly sensitive strain sensors, Mater. Design 143 (2018) 214–223.
[20] K. Huang, S. Dong, J. Yang, J. Yan, Y. Xue, X. You, J. Hu, L.e. Gao, X. Zhang, Y. Ding, Three-dimensional printing of a tunable graphene-based elastomer for strain sensors with ultrahigh sensitivity, Carbon 143 (2019) 63–72.
[21] W. Zhang, J. Suhr, N. Koratkar, Carbon nanotube/polycarbonate composites as multifunctional strain sensors, J. Nanosci. Nanotechnol. 6 (4) (2006) 960–964.
[22] N. Hu, Y. Karube, M. Arai, T. Watanabe, C. Yan, Y. Li, Y. Liu, H. Fukunaga, Investigation on sensitivity of a polymer/carbon nanotube composite strain sensor, Carbon 48 (3) (2010) 680–687.
[23] K. Parmar, M. Mahmoodi, C. Park, S.S. Park, Effect of CNT alignment on the strain sensing capability of carbon nanotube composites, Smart Mater. Struct. 22 (2013) 075006.
[24] H. Tanabi, M. Erdal, Effect of CNTs dispersion on electrical, mechanical and strain sensing properties of CNT/epoxy nanocomposites, Results Phys. 12 (2019) 486–503.
[25] B. Hu, N. Hu, Y. Li, K. Akagi, W. Yuan, T. Watanabe, Y. Cai, Multi-scale numerical simulations on piezoresistivity of CNT/polymer nanocomposites, Nanoscale Res. Lett. 7 (2012) 1–11.
[26] M.A.S. Matos, V.L. Tagarielli, P.M. Baiz-Villafranca, S.T. Pinho, Predictions of the electro-mechanical response of conductive CNT-polymer composites, J. Mech. Phys. Solids 114 (2018) 84–96.
[27] H. Yang, L. Yuan, X.F. Yao, D.N. Fang, Piezoresistive response of graphene rubber composites considering the tunneling effect, J. Mech. Phys. Solids 139 (2020) 103943.
[28] X.D. Xia, S.J. Zhao, C. Fang, G.J. Weng, Modeling the strain-dependent electrical resistance and strain sensitivity factor of CNT-polymer nanocomposites, Math. Method. Appl. Sci. (2020) 1–15.
[29] Y. Fang, L.Y. Li, S.H. Jang, Piezoresistive modelling of CNTs reinforced composites under mechanical loadings, Compos. Sci. Technol. 208 (2021) 108757.
[30] C. Zhao, W. Yuan, H. Liu, B. Gu, N. Hu, Alamusi, Y. Ning, F. Jia, Equivalent circuit model for the strain sensing characteristics of multi-walled carbon nanotube/polyvinylidene fluoride films in alternating current circuit, Carbon 129 (2018) 585–591.
[31] K. Huang, H. Ning, N. Hu, X. Wu, S. Wang, S. Weng, W. Yuan, Alamusi, L. Wu, Y. Liu, Synergistic effect of CB and MWCNT on the strain-induced DC and AC electrical properties of PVDF-HFP composites, Carbon 144 (2019) 509–518.
[32] J.C. Dyre, A simple model of ac hopping conductivity in disordered solids, Phys. Lett. A 108 (9) (1985) 457–461.
[33] J.C. Maxwell, A treatise on electricity and magnetism, 3rd ed., Clarendon Press, Oxford, 1982.
[34] K.W. Wagner, The after effect in dielectrics, Arch. Electrotech 2 (1914) 378–394.
[35] R.W. Sillars, The properties of a dielectric containing semiconducting particles of various shapes, Inst. Elec. Eng. - Proc. Wireless Sect. 12 (1937) 139–155.
[36] P. Debye, Results of a kinetic theory of dielectrics, Phys. Z 13 (1912) 976–1000.
[37] M.A. Poothanari, J. Abraham, N. Kalarikkal, S. Thomas, Excellent Electromagnetic Interference Shielding and High Electrical Conductivity of Compatibilized Polycarbonate/Polypropylene Carbon Nanotube Blend Nanocomposites, Ind. Eng. Chem. Res. 57 (12) (2018) 4287–4297.
[38] H. Rezvantalab, N. Ghazi, M.J. Ambrusch, J. Infante, S. Shojaei-Zadeh, An aqueous-based approach for fabrication of PVDF/MWCNT porous composites, Scientific reports 7 (2017) 1–10.
[39] Twinkle, M. Kaur, J.K. Gowsamy, P. Kumar, S. Kumar, Synthesis and characterization of CNT/PVDF paper for electronic and energy storage applications, Emergent Mater. 3 (2) (2020) 181–185.
[40] B.V. Basheer, J.J. George, S. Siengchin, J. Parameswaranpillai, Polymer grafted carbon nanotubes—Synthesis, properties, and applications: A review, Nano-Struct. Nano-Objects 22 (2020) 100429, https://doi.org/10.1016/j.nanoso.2020.100429.
[41] N. Chikyu, T. Nakano, G. Kletetschka, Y. Inoue, Excellent electromagnetic interference shielding characteristics of a unidirectionally oriented thin multiwalled carbon nanotube/polyethylene film, Mater. Design 195 (2020) 108918.
[42] P. Saxena, P. Shukla, A comprehensive review on fundamental properties and applications of poly (vinylidene fluoride)(PVDF), Adv. Compos. Hybrid Mater. 4 (1) (2021) 8–26.
[43] R. Hill, Theory of mechanical properties of fiber-strengthened materials: I. Elastic behavior, J. Mech. Phys. Solids 13 (1964) 89–101.
[44] L.J. Walpole, Elastic behavior of composite materials: theoretical foundations, Adv. Appl. Mech. 21 (1981) 169–242.
[45] G.P. Tandon, G.J. Weng, A theory of particle-reinforced plasticity, J. Appl. Mech. 55 (1988) 126–135.
[46] I.J. Beyerlein, M.J. Demkowicz, A. Misra, B.P. Uberuaga, Defect-interface interactions, Prog. Mater. Sci. 74 (2015) 125–210.
[47] X. Xia, Z. Zhong, G.J. Weng, Maxwell–Wagner–Sillars mechanism in the frequency dependence of electrical conductivity and dielectric permittivity of graphene-polymer nanocomposites, Mech. Mater. 109 (2017) 42–50.
[48] Y. Wang, G.J. Weng, S.A. Meguid, A.M. Hamouda, A continuum model with a percolation threshold and tunneling-assisted interfacial conductivity for carbon nanotube-based nanocomposites, J. Appl. Phys. 115 (2014) 193706.
[49] L.D. Landau, E.M. Lifshitz, L.P. Pitaevskii, Electrodynamics of continuous media, 3rd ed., Pergamon Press, New York, 1984.
[50] G.J. Weng, A dynamical theory for the Mori-Tanaka and Ponte Castañeda-Willis estimates, Mech. Mater. 42 (9) (2010) 886–893.
[51] Y.P. Qiu, G.J. Weng, On the application of Mori-Tanaka's theory involving transversely isotropic spheroidal inclusions, Int. J. Eng. Sci. 28 (11) (1990) 1121–1137.
[52] G. Hu, A method of plasticity for general aligned spheroidal void or fiber-reinforced composites, Int. J. Plasticity 12 (1996) 439–449.
[53] X.D. Xia, B.X. Xu, X.Z. Xiao, G.J. Weng, Modeling the dielectric breakdown strength and energy storage density of graphite-polymer composites with dielectric damage process, Mater. Design 189 (2020) 108531.
[54] G. Yin, N. Hu, Y. Karube, Y. Liu, Y. Li, H. Fukunaga, A carbon nanotube/polymer strain sensor with linear and anti-symmetric piezoresistivity, J. Compos. Mater. 45 (2011) 1315–1323.
[55] S.K. Yadav, S.S. Mahapatra, J.W. Cho, Tailored dielectric and mechanical properties of noncovalently functionalized carbon nanotube/poly (styrene-b-(ethylene-co-butylene)-b-styrene) nanocomposites, J. Appl. Polym. Sci. 129 (4) (2013) 2305–2312.
[56] S. Tong, W. Yuan, H. Liu, N. Hu, C. Zhao, Y. Zhao, Linear strain sensor made of multi-walled carbon nanotube/epoxy composite, Mater. Res. Express 4 (2017) 115008.